Article:

Kazemisangdehi, S. orcid.org/0000-0002-0174-6643, Zhu, Z.Q. orcid.org/0000-0001-7175-3307, Chen, L. et al. (2 more authors) (2025) Novel hybrid rare-earth and ferrite magnet asymmetric V-shape and U-shape IPMSMs accounting for demagnetisation withstand capability. IET Electric Power Applications, 19 (1). e70054. ISSN 1751-8660

https://doi.org/10.1049/elp2.70054

IET Electric Power Applications

WILEY

The Institution of Engineering and Technology

ORIGINAL RESEARCH OPEN ACCESS

Novel Hybrid Rare-Earth and Ferrite Magnet Asymmetric V-Shape and U-Shape IPMSMs Accounting for Demagnetisation Withstand Capability

Seyedmilad Kazemisangdehi[1] | Zi Qiang Zhu[1] | Liang Chen[2] | Lei Yang[2] | Yanjian Zhou[2]

[1]Department of Electronic and Electrical Engineering, University of Sheffield, Sheffield, UK | [2]The Midea Group Corporate Research Center, Shanghai, China

Correspondence: Zi Qiang Zhu (z.q.zhu@sheffield.ac.uk)

Received: 27 February 2025 | **Revised:** 22 April 2025 | **Accepted:** 26 May 2025

Handling Editor: Udochukwu Bola Akuru

Funding: This work is supported by the Midea Group, P. R. China under R/174939-11-1.

Keywords: cost reduction | permanent magnet machines | permanent magnet motors | synchronous machines | synchronous motors

ABSTRACT

This paper presents two novel hybrid rare-earth and ferrite permanent magnet (HPM) asymmetric V-shape and U-shape interior PM synchronous machines (IPMSMs) with high ferrite PM (FEPM) torque contribution accounting for the enhanced demagnetisation withstand capability of FEPM at both open circuit and overload conditions. The proposed topologies are designed and compared with a rare-earth PM (REPM)-based symmetrical V-shape baseline in terms of electromagnetic performances, mechanical strength, demagnetisation withstand capability, and PMs cost. All machines are optimised for the same torque with the minimum volume of high-cost REPM at the same specification and size as a commercialised electric vehicle (EV) IPMSM. It is shown that the synergies of magnetic field shifting effect and HPM utilisation have improved the torque per REPM usage in both proposed machines. However, the magnetic field shifting of the proposed HPM asymmetric U-shape IPMSM is twice of that in the V-shape IPMSM counterpart along with a slightly better FEPM demagnetisation withstand capability. Meanwhile, the results show that the proposed HPM asymmetric V-shape IPMSM would be cheaper than the U-shape counterpart as the former and latter topologies require ~31% and ~23.5% less REPM volume than the baseline, respectively. Finally, two small laboratory size prototypes are made and tested to verify the finite element analyses.

1 | Introduction

The rare-earth permanent magnet (REPM) machines with outstanding benefits of high torque/power densities and high efficiency etc. have been widely used in high performance electric vehicles (EVs) [1]. Meanwhile, as the EV market is growing, a cost-effective design challenge has been raised towards the electrification transportation. On the one hand, the competitive EV market has required the US Department of Energy (DoE) and the UK Advanced Propulsion Centre (APC) to draft higher performance targets for the future [2]. On the other hand, the DoE has reported that about 20%–30% of total expense of a PM machine belongs to the price of the costly REPMs [3]. To address this issue, the torque per REPM volume ratio needs to be improved in PM machines [4].

The magnetic field shifting effect in an asymmetric rotor geometry and the utilisation of low-cost ferrite PMs (FEPMs) in a hybrid PM (HPM) configuration are the two promising examples of torque per REPM volume ratio enhancement methods which have gained a lot of attention in recent years [5, 6]. In an asymmetric rotor PM machine, the reduced difference between the corresponding current advancing angles of the maximum PM and reluctance torque components leads to a higher resultant torque [7]. For example, an additional flux barrier is used in an asymmetric V-shape IPMSM to enhance the output torque by improving the magnetic field shifting effect of the proposed machine in Ref. [8].

Meanwhile, the main feature of the HPM machines relies on using the high-energy product but expensive REPMs together with the low-energy product but inexpensive FEPMs in one topology. As a result, these machines can deliver a high performance at a reduced cost. The HPM utilisation can be considered as a new approach in the design of PM machines which is introduced only about a dozen of years ago [6, 9–11]. These machines can be divided into three configurations, including parallel, series, and mixed which are categorised by the relative positions of two PM materials in an equivalent magnetic circuit [12]. For example, the flux paths of two PM types are in parallel in a parallel HPM configuration. Therefore, each PM type would face a lower magnetic reluctance in its flux path leading to a higher electromagnetic performance than an equivalent series HPM counterpart. On the downside, a parallel HPM arrangement suffers from a lower demagnetisation withstand capability of FEPMs than a series HPM topology [11, 13]. Meanwhile, a mixed HPM configuration is a combination of the first two designs and has a traded-off performance [14].

The effect of the difference in the magnetic properties of two PM types on the electromagnetic performance of HPM machines at different working conditions is investigated during the optimisation for EV application in Refs. [15, 16]. Meanwhile, unlike the REPMs, FEPMs will be more vulnerable to the irreversible demagnetisation at low temperatures due to having different alpha coefficients with opposite signs. Therefore, the demagnetisation withstand capabilities of REPMs and FEPMs will be investigated at high and low temperatures, respectively [17]. It is shown in Ref. [18] that a spoke-type IPMSM with a parallel configuration of HPM can significantly improve the torque per REPM volume ratio of PM machines due to the high consumption of FEPMs in each spoke. Meanwhile, a novel parallel HPM V-shape spoke IPMSM is introduced in Ref. [19] to not only maximise the FEPM usage in each spoke, but also improve the reluctance torque component by using a V-shape arrangement.

Although each of these methods can separately improve the torque per REPM ratio in a PM machine, a combination of them may lead to even more enhanced benefits. For example, the application of an asymmetric bar-shape REPM in a series and a mixed HPM spoke-type IPMSMs are investigated in Refs. [12, 15, 20, 21], respectively. The proposed machines in both configurations are shown to have an enhanced torque density due to the magnetic field shifting effect. In Ref. [22], a novel asymmetric HPM assisted synchronous reluctance machine is proposed to improve the magnetic field shifting effect with a multi-layer arrangement of PMs. In addition, an asymmetric HPM machine with unequal north and south poles is proposed in Ref. [23]. Although the performance is improved, this machine may suffer from the axial leakage flux due to the employment of unequal poles. In Ref. [24], a HPM IPMSM with a consequent pole asymmetric rotor structure is compared to a conventional pole asymmetric rotor counterpart. The results show that the proposed consequent pole IPMSM benefits from a higher torque per REPM volume ratio than its conventional counterpart at the cost of slightly lower overload capability and having no magnetic field shifting effect. In Ref. [25], a novel HPM asymmetric V-shape IPMSM is proposed which benefits from an improved torque compared to the other topologies. However, the torque per cost ratio of the proposed machine is only reduced by 2% compared to that of the REPM-based asymmetric V-shape IPMSM counterpart due to the low utilisation of FEPMs. Similarly, a small segment of FEPM per pole with low torque contribution is proposed in an asymmetric HPM V-shape IPMSM in Ref. [26].

This paper proposes two mixed parallel and series HPM asymmetric V-shape and U-shape IPMSMs with high contribution of FEPMs with a due account for the improved demagnetisation withstand capability of these magnets. It will be shown that the proposed HPM machines can effectively reduce the required volume of REPM by improving the FEPM usage and magnetic field shifting. Unlike the literature, the proposed V-shape structure utilises a simple V-shape arrangement of PMs with a large FEPM segment and no extra flux barrier. Meanwhile, the proposed U-shape counterpart consists of a novel L-shape arrangement of PMs in a U-shape flux barrier design. It will be shown that the proposed mixed HPM asymmetric V-shape IPMSM benefits from an intermediate magnetic field shifting effect compared to the maximised magnetic field shifting effect of the U-shape counterpart. Meanwhile, the FEPM torque contribution of the V-shape design is higher than that of the U-shape counterpart. However, unlike the low FEPM torque contribution in literature, the FEPM torque contribution in both machines are considerable compared to their REPM torque components.

From the demagnetisation point of view, the vulnerable locations for FEPM usage are detected in both HPM asymmetric designs. Therefore, removing the FEPMs from the prohibited area to enhance the demagnetisation withstand capability leads to the structural modification of the proposed HPM asymmetric V-shape and U-shape IPMSMs. The V-shape topology employs an enlarged barrier over FEPM to distance this magnet from the armature current. Meanwhile, the vulnerable FEPM in U-shape counterpart is removed which converts the U-shape arrangement of PMs into the new L-shape structure which results in improving the demagnetisation withstand capability and the magnetic field shifting effect. As will be shown, the demagnetisation withstand capability of FEPMs is considerably improved in both proposed HPM machines under the extreme demagnetisation conditions at both open circuit and overload operations. Meanwhile, it should be noted that the improved demagnetisation is achieved at the cost of a slight reduction of torque performance which can be interpreted as a slight increase in the cost of PMs for generating the same torque. A detailed comparison will be investigated including the electromagnetic performance at the open-circuit and on-load conditions, loss/efficiency maps, and torque component decomposition using the frozen permeability method in Ref. [27].

In this regard, Section 2 introduces the initial (V-1 and U-1) and final (V-2 and U-2) proposed mixed parallel and series HPM asymmetric V-shape and U-shape IPMSMs and the REPM-based symmetrical V-shape IPMSM as the baseline. In Section 3, the finite element analysis (FEA) is employed to investigate and compare the electromagnetic performances, mechanical strengths, and the demagnetisation withstand capabilities, whereas in Section 4 a comparison of PM cost is presented. Finally, Sections 5 and 6 summarise the experimental validation and conclusion, respectively.

2 | Mixed Parallel and Series HPM Asymmetric V-Shape and U-Shape IPMSMs

As this study only focuses on the design of different rotor geometries, the same specifications and stator of a commercialised EV IPMSM is used as presented in Table 1 and Figure 1a. As can be seen this machine produces 280 Nm peak torque at 625 A_{max} and 2100 r/min.

The V-shape IPMSMs are known for their simple structure with increased saliency and flux focusing effect. Therefore, the baseline of this study is designated as a REPM-based symmetrical V-shape IPMSM using the NdFeB type N28AH, as shown Figure 1b. Then, two initial mixed parallel and series HPM asymmetric IPMSMs, that is, V-1 and U-1 (see Figure 1c,d), and two final mixed parallel and series HPM asymmetric IPMSMs, that is, V-2 and U-2 (see Figure 1e,f), without and with considering the demagnetisation withstand capability of FEPMs will be designed using the same REPM material and FEPM type TDK-FB13B. The main design criterion of all these HPM machines is to achieve the same torque as the baseline with a lower volume of REPM by substituting a part of this magnet with FEPM. For the sake of comparison, the inner and our radii of rotor, the stack length, the airgap length, the stator dimensions, and the winding configurations are kept constant. Therefore, only the rotor structures will be re-designed. It is also worth mentioning that as can be seen in Figure 1c–f, all HPM asymmetric IPMSMs presented in this paper can be categorised in Group 4 of the asymmetric IPMSM classification in Ref. [5], where both PM configuration and rotor core structure are asymmetric.

Figure 2 presents a flowchart of the design procedure employed in this paper. As can be seen, at first, the topologies of the mixed parallel and series HPM asymmetric V-1 and U-1 IPMSMs with two segments of FEPMs per pole are selected to be optimised for 280 Nm torque with lower volume of REPM at 625 A_{max} and 2100 r/min. These topologies enable a high utilisation of FEPM and its resultant torque contribution. As will be shown by the optimisation and FEA results, the required volume of REPM can be considerably reduced when the demagnetisation withstand capability is not considered. This is to evaluate the maximum reduction of REPM usage and PM cost saving. Meanwhile, the analysis of demagnetisation withstand capability shows that the small segments of FEPM will be at a high risk of irreversible demagnetisation at both open-circuit and overload conditions. Consequently, accounting for the demagnetisation withstand capability improvement of FEPMs, the modified topologies, that is, mixed parallel and series HPM asymmetric V-2 and U-2 IPMSMs are proposed and optimised with the same objectives. This is to evaluate the difference in the

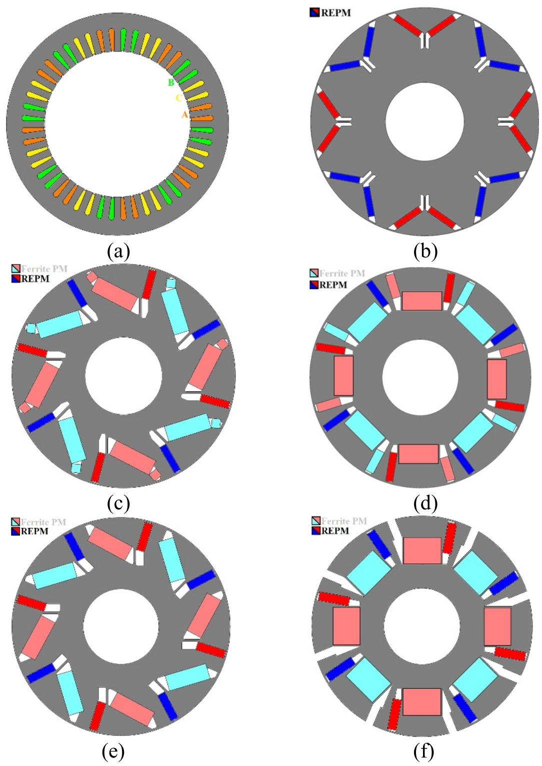

FIGURE 1 | Structural comparison of IPMSMs. (a) Stator of the commercialised EV IPMSM. (b) REPM-based symmetrical V-shape rotor (baseline). (c) HPM asymmetric V-1 rotor (initial design). (d) HPM asymmetric U-1 rotor (initial design). (e) HPM asymmetric V-2 rotor (proposed final design). (f) HPM asymmetric U-2 rotor (proposed final design).

TABLE 1 | Specifications of commercialised IPMSM.

Parameters	Values	Parameters	Values
Stator slot no.	48	Peak speed (r/min)	10,000
Rotor pole no.	8	Rated speed (r/min)	2100
Stator outer diameter (mm)	200	Peak torque (Nm)	280
Stator inner diameter (mm)	131	Peak current (A_{max})	625
Rotor outer diameter (mm)	130	Conductor no. per slot	8
Rotor inner diameter (mm)	45	Number of parallel branches	4
Stack length (mm)	151	NdFeB remanence (T)	1.075
Airgap length (mm)	0.5	Angle of step skew with 3 steps (degree)	3.75

required volume of REPM and PM cost saving without and with considering the demagnetisation withstand capability improvement of FEPMs. These machines are introduced in more detail in Sections 2.1–2.5.

For convenience, in the following discussions, all IPMSMs will have 'mixed parallel and series HPMs' and hence 'mixed parallel and series HPM IPMSMs' will be simply designated as 'HPM IPMSMs'.

2.1 | REPM-Based Symmetrical V-Shape IPMSM (Baseline)

A REPM-based symmetrical V-shape IPMSM is considered as the baseline of this study. The baseline uses neither the magnetic field shifting effect nor the HPM utilisation. Therefore, it is expected to have the highest required volume of REPMs among all topologies in Figure 1. Therefore, it will be used as the REPM usage limit during the optimisation of others.

2.2 | HPM Asymmetric V-1 IPMSM

The optimum design of the HPM asymmetric V-1 IPMSM with two FEPM segments is presented in Figure 1c. This machine maximises the utilisation of FEPMs along with a decent magnetic field shifting effect. As a result, a high reduction of REPM usage is expected. As can be seen, the REPM is in parallel to the two FEPM segments within 1 pole. However, considering two adjacent poles, the two PM types are in a series connection. Therefore, the overall configuration of HPM in this machine is considered as mixed (a combination of the series and parallel HPM configurations).

2.3 | HPM Asymmetric U-1 IPMSM

Similar to the HPM asymmetric V-1 IPMSM, a HPM counterpart with the U-shape arrangement of PMs and two FEPM segments per pole is optimised as shown in Figure 1d. The configuration of HPM is also considered as mixed.

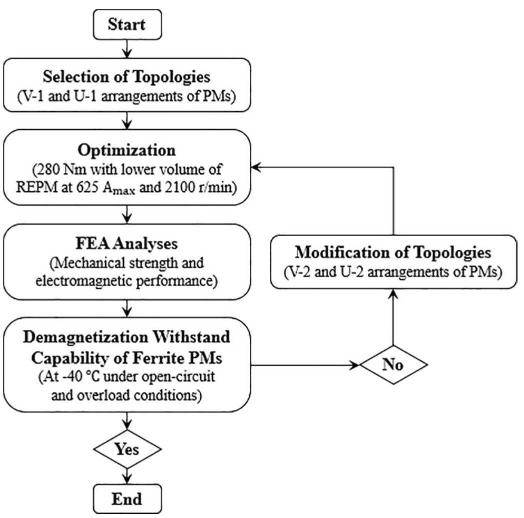

FIGURE 2 | Flowchart of the employed design procedure.

2.4 | HPM Asymmetric V-2 IPMSM

Accounting for the demagnetisation withstand capability of FEPMs, it will be shown that the small FEPM in the mixed HPM asymmetric V-1 IPMSM suffers from a high risk. As a result, this magnet needs to be removed at the cost of a torque reduction. Therefore, the HPM asymmetric V-2 IPMSM is optimised with 1 FEPM segment per pole as shown in Figure 1e. It will be shown that this machine benefits from a higher demagnetisation withstand capability at the cost of an increased volume of REPM than those of the V-1 counterpart.

2.5 | HPM Asymmetric U-2 IPMSM

Similarly, the FEPM segment on the side of the HPM asymmetric U-1 IPMSM suffers from a high demagnetisation risk. Therefore, the proposed HPM asymmetric U-2 IPMSM is designed and optimised as shown in Figure 1f. It will be shown that this machine benefits from a higher demagnetisation withstand capability at the cost of an increased volume of REPM than those of the U-1 counterpart.

2.6 | Theoretical Analysis of Magnetic Field Shifting Effect

In this subsection, the principle of the magnetic field shifting effect in asymmetric IPMSMs will be discussed by employing a simplified analytical model without considering saturation, cross-magnetisation, and harmonics [5].

On the one hand, Figure 3 compares the vector diagrams of stator current and PM flux linkage in symmetrical and asymmetric IPMSMs in the dq-axis coordinates. In this figure, i_s, i_d, and i_q are the vectors of stator and dq-axis currents. Similarly, Ψ_{pm}, Ψ_{fd}, and Ψ_{fq} are the vectors of resultant PM flux linkage, and dq-axis flux linkages, respectively. Finally, β is the current advancing angle in both machines, and α_s is the asymmetric angle in asymmetric IPMSM only.

On the other hand, the dq-axis flux linkages can be generally written as follows:

$$\begin{cases} \Psi_d = \Psi_{fd} + L_d i_d \\ \Psi_q = \Psi_{fq} + L_q i_d, \end{cases} \tag{1}$$

where Ψ_d and Ψ_q are the dq-axis PM flux linkages, and L_d and L_q are the dq-axis inductances, respectively.

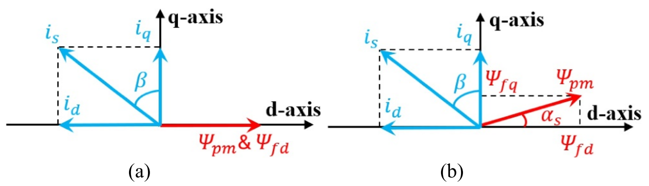

FIGURE 3 | Comparison of vector diagrams in dq-axis coordinates. (a) Symmetrical IPMSM. (b) Asymmetric IPMSM.

Therefore, considering Figure 3 and Equation (1), the equation of Ψ_d and Ψ_q for the symmetrical and asymmetric IPMSMs can be re-written as Equations (2) and (3), respectively:

$$\begin{cases} \Psi_d = \Psi_{\text{pm}} - L_d i_s \sin\beta \\ \Psi_q = L_q i_s \cos\beta \,, \end{cases} \tag{2}$$

$$\begin{cases} \Psi_d = \Psi_{\text{pm}} \cos\alpha_s - L_d i_s \sin\beta \\ \Psi_q = \Psi_{\text{pm}} \sin\alpha_s + L_q i_s \cos\beta. \end{cases} \tag{3}$$

Meanwhile, considering a PM torque component corresponding to the interaction of q-axis flux linkage (Ψ_{fq}) and d-axis current (i_d), the output torque of an IPMSM (T_{out}) can generally be written as a summation of PM torque (T_m) and reluctance torque (T_r) as follows:

$$T_{\text{out}} = T_m + T_r = \frac{3p}{2}\left(\left(\psi_{fd} i_q + \psi_{fq} i_d\right) + \left(L_d - L_q\right) i_d i_q\right), \tag{4}$$

where p is the number of pole pairs.

Finally, by substituting Equations (2) and (3) into Equation (4), and after simplification, the output torques of the symmetrical ($T_{\text{out-IPMSM}}$) and the asymmetric ($T_{\text{out-AIPMSM}}$) IPMSMs can be expressed as Equation (5) [5]:

$$\begin{cases} T_{\text{out-IPMSM}} = T_{\text{pm}} \cos\beta + T_{\text{rel}} \sin 2\beta \\ T_{\text{out-AIPMSM}} = T_{\text{pm}} \cos(\beta - \alpha_s) + T_{\text{rel}} \sin 2\beta, \end{cases} \tag{5}$$

where T_{pm} and T_{rel} are the amplitudes of PM and reluctance torque component which can be shown as follows:

$$\begin{cases} T_{\text{pm}} = \dfrac{3p}{2}\,\Psi_{\text{pm}} i_s \\ T_{\text{rel}} = \dfrac{3p}{4}\left(L_q - L_d\right) {i_s}^2. \end{cases} \tag{6}$$

In theory by assuming that the peak reluctance torque component of an IPMSM reaches at β = 45 Elec. Deg., it can be concluded from Equation (5) that the PM torque component of a symmetrical IPMSM reach its maximum at $\beta = 0$. Meanwhile, that of an asymmetric IPMSM happen at $\beta = \alpha_s$. Therefore, the current advancing angle difference ($\Delta\beta$) between the maximum PM torque and reluctance torque components of an asymmetric IPMSM is less than that of the symmetrical IPMSM counterpart with a positive α_s due to the magnetic field shifting effect. It means, the resultant torque of an asymmetric IPMSM can be improved even with the same PM and reluctance torque amplitudes. In other words, an asymmetric IPMSM can generate the same torque as a symmetrical IPMSM with even lower electric and magnetic loadings.

It is also worth adding that in an asymmetric HPM machine, Ψ_{pm} will be generated by two PM types, that is, REPM and FEPM.

3 | Finite Element Results

The FEA predicted results are presented in this section. The aim is to improve the torque per REPM volume ratio of the proposed HPM machines by combining the HPM utilisation and the magnetic field shifting effect. In this paper, the optimisation is conducted when the genetic algorithm (GA) within ANSYS Maxwell FEA software is used to optimise the rotor in each topology. All these HPM machines are optimised to deliver the same torque (280 Nm) as the baseline with a lower volume of REPM at 625 A_{max} and 2100 r/min. Meanwhile, the torque ripple mitigation is considered as the second objective. As there are more than one objective, the optimisation function can be written as follows:

$$\begin{cases} \text{Objectives: Max}\left[T_{\text{out}}\right],\ \text{Min}\left[V_{\text{NdFeB}}\right],\ \text{Min}\left[T_{\text{ripple}}\right] \\ \text{Constraints: } T_{\text{out}} \geq 280\ \text{Nm},\ V_{\text{NdFeB}} \leq 150.2\ \text{cm}^3, \\ \text{Weighting factors: } K_{T_{\text{out}}} = 4\text{p.u.},\ K_{V_{\text{NdFeB}}} = 2\text{p.u.},\ K_{T_{\text{ripple}}} = 1\text{p.u.} \\ \text{Variables: listed in Tables 2 and 3.} \end{cases} \tag{7}$$

where T_{out}, V_{NdFeB}, and T_{ripple} are the output torque, the volume of REPM, and the torque ripple, respectively.

Therefore, at a fair condition by using the same size and torque, the optimisation results will reveal the reduced amount of REPM volume and the cost of PMs. Then, a demagnetisation withstand capability study will be conducted to investigate the risk of damage to the magnets at severe demagnetisation conditions. Moreover, a detailed comparison of performance in all machines will be conducted to compare their features and explain how the REPM usage and PM cost can be reduced at the same performance in the proposed HPM asymmetric IPMSMs accounting for an improved demagnetisation withstand capability. Meanwhile, having a similar mechanical strength is considered as a precondition for a fair comparison.

3.1 | Optimisation Results (Baseline, HPM Asymmetric V-1, and U-1)

The optimisation results of the baseline, HPM asymmetric V-1 and U-1 IPMSMs will be discussed in this subsection when they are optimised with the above-mentioned objectives. Figure 4a presents the parametric model of the REPM-based symmetrical V-shape IPMSM (baseline), whereas the optimisation result, and the optimum cross section are shown in Figure 4b,c, respectively. As can be seen, this machine requires ~150.2 cm^3 volume of REPM to deliver 280 Nm peak torque at 625 A_{max} and 2100 r/min.

Meanwhile, Figure 5a–c presents the parametric model of the HPM asymmetric V-1 IPMSM, the optimisation result and the optimum cross section, respectively. As can be seen, this machine only needs ~87.3 cm^3 volume of REPM to generate the same torque which results in the reduction of REPM volume by ~42% compared to the baseline. In general, by using FEPM on one side and REPM on the other side of a V-shape structure, an asymmetric rotor can be achieved which is due to the difference in the residual flux densities of these two PM types. However, two specific design considerations are used to effectively increase the magnetic field shifting effect. Firstly, the relative angles of REPM and FEPM which are used to define their arcs, can be changed independently. Secondly, the centre of the V-shape structure can be displaced in Y-axis as shown in

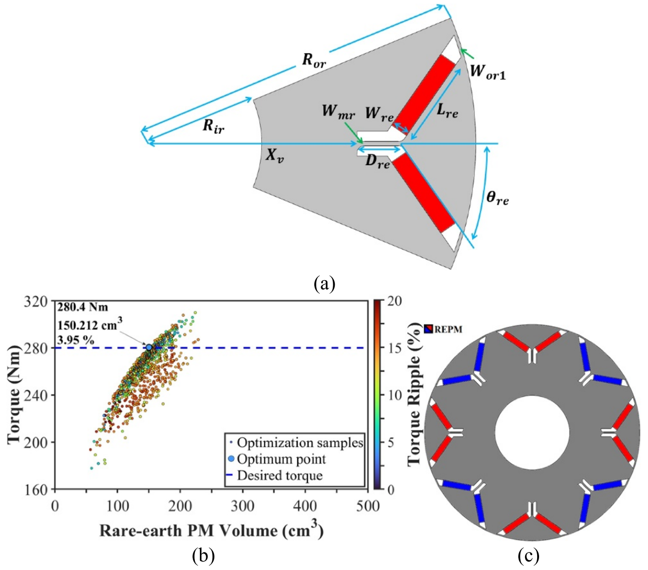

FIGURE 4 | REPM-based symmetrical V IPMSM (baseline). (a) Parametric model. (b) Optimisation result at 625 A_{max} and 2100 r/min. (c) Optimum cross section.

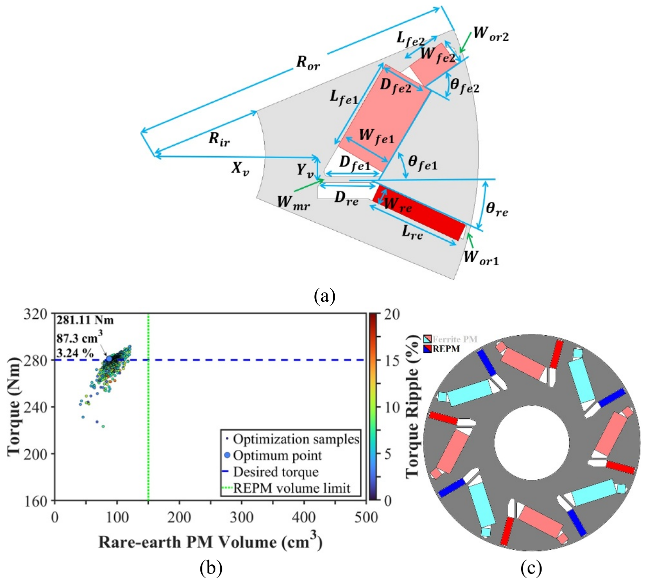

FIGURE 5 | HPM asymmetric V-1 IPMSM. (a) Parametric model. (b) Optimisation result at 625 A_{max} and 2100 r/min. (c) Optimum cross section.

Figure 5a. As will be shown, a displaced centre of V-shape arrangement causes an intentional saturation between two adjacent poles which helps with the magnetic field shifting.

Finally, Figure 6a–c presents the parametric model, optimisation results, and optimum cross section of the HPM asymmetric U-1 IPMSM, respectively.

As can be seen, to generate 280 Nm torque at 625 A_{max} and 2100 r/min, ~89.3 cm^3 volume of REPM is consumed in this structure. Therefore, at the same torque and size, the volume of high-cost REPM can be reduced by ~40.5%. It is worth mentioning that for this design, two parameters are added to

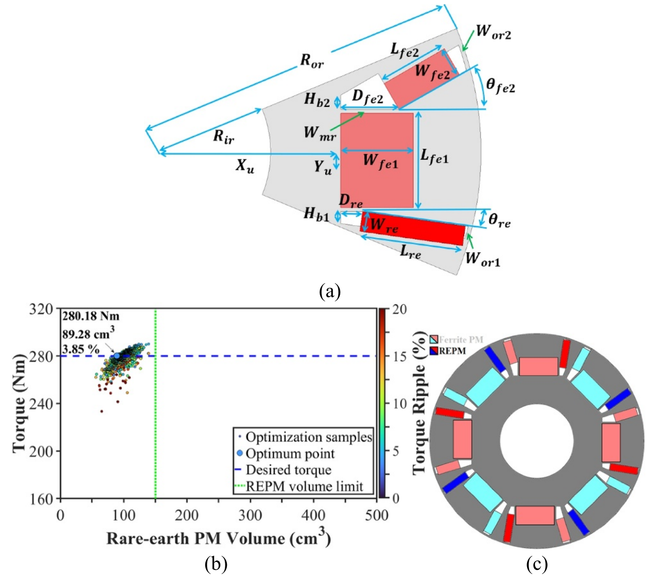

FIGURE 6 | HPM asymmetric U-1 IPMSM. (a) Parametric model. (b) Optimisation result at 625 A_{max} and 2100 r/min. (c) Optimum cross section.

independently optimise the height of air barriers (H_{b1} and H_{b2}) as shown in Figure 6a. This is to add more flexibility to cause an intentional saturation between two adjacent poles with the aim of improving the magnetic field shifting. Table 2 summarises the definitions and the optimum values of the design parameters in these three machines. All parameters listed in this table are considered as the optimisation variables except the constant inner and outer radii of rotor. Meanwhile, the widths of the ribs are defined using the mechanical strength analysis using the von-mises stress distributions at 10 kr/min rotor speed as shown in Figure 7.

This is to achieve a similar von-mises stress on the ribs to ensure a fair comparison of the performances and the PM usage. Generally, the mechanical strength of rotor can be considered as an important factor when utilising the HPMs. This is because replacing a certain amount of REPM at the same performance requires a higher volume of FEPM due to the difference in the magnetic properties of these two magnet types. Consequently, the increased mass of PMs can potentially transfer more stress on ribs. Therefore, the widths of the ribs need to be adjusted for the similar performance and mechanical strength considering that a thicker width, a higher leakage flux and thus a higher required volume of REPM. Consequently, the adjusted widths of the ribs for a similar maximum von-mises stress level is considered as a pre-condition of a fair PM usage comparison. As can be seen, the maximum stress on rib in these topologies can reach ~240 MPa which implies the safety factor of ~1.9 at the maximum speed. It is worth mentioning that the frictional contact with a friction coefficient of 0.2 is used for this analysis.

3.2 | Comparison of HPM Asymmetric V-1 and U-1 IPMSMs

Figure 8 compares the open circuit flux density and flux line distributions of the HPM asymmetric V-1 and U-1 IPMSMs. As

TABLE 2 | Design parameters of baseline, V-1 and U-1 IPMSMs.

Parameter	REPM-based symmetrical V	HPM asymmetric V-1	HPM asymmetric U-1
Rotor outer radius (R_{or})—mm		65	
Rotor inner radius (R_{ir})—mm		22.5	
V-shape in x-axis (X_v)—mm	41.4	33.42	—
V-shape in y-axis (Y_v)—mm	0	9.75	—
U-shape in X-axis (X_u)—mm	—	—	39.45
U-shape in Y-axis (Y_u)—mm	—	—	**1.02**
Width of REPM (W_{re})—mm	3.63	4.21	4.32
Length of REPM (L_{re})—mm	17.13	17.18	17.11
Width of FEPM1 (W_{fe1})—mm	—	9.23	11.24
Length of FEPM1 (L_{fe1})—mm	—	25.81	23.29
Width of FEPM2 (W_{fe2})—mm	—	5.46	5.2
Length of FEPM2 (L_{fe2})—mm	—	4.94	14.04
Angle of REPM (θ_{re})—Degree	55.13	14.91	9.04
Angle of FEPM1 (θ_{fe1})—Degree	—	62.63	—
Angle of FEPM2 (θ_{fe2})—Degree	—	66.29	17.13
REPM displacement (D_{re})—mm	6.05	11.04	5.14
FEPM1 displacement (D_{fe1})—mm	—	9.82	—
FEPM2 displacement (D_{fe2})—mm	—	8.95	8.41
Height of barrier 1 (H_{b1})—mm	—	—	2.46
Height of barrier 2 (H_{b2})—mm	—	—	2.86
Width of middle rib (W_{mr})—mm	0.8	1.2	0.8
Width of outer rib 1 (W_{or1})—mm	0.6	0.8	0.8
Width of outer rib 2 (W_{or2})—mm	—	1.2	0.8

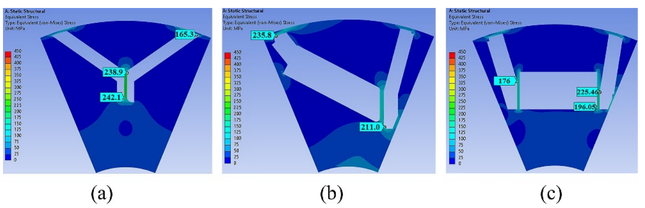

FIGURE 7 | Comparison of von-mises stress distributions at 10 kr/min. (a) REPM-based symmetrical V IPMSM. (b) HPM asymmetric V-1 IPMSM. (c) HPM asymmetric U-1 IPMSM.

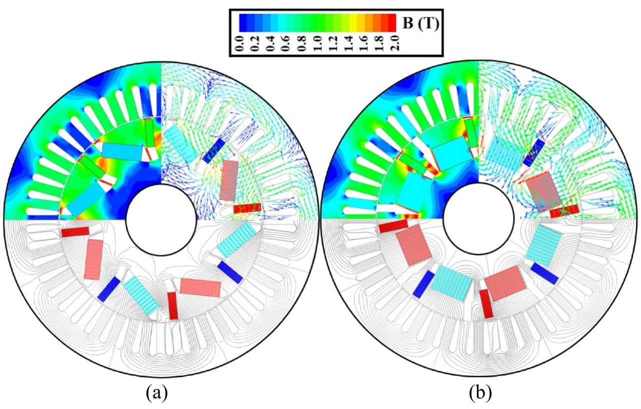

FIGURE 8 | Comparison of open circuit flux density and flux line distributions. (a) HPM asymmetric V-1 IPMSM. (b) HPM asymmetric U-1 IPMSM.

can be seen, the d-axis is shifted in both machines. In addition, by focusing on the flux lines, the series connection of HPMs between two adjacent poles is visible. The comparison of the open circuit airgap flux density waveforms, spectra, and fundamental component waveforms can be found in Figure 9a–c, respectively. As suggested by Ref. [7], a numerical comparison of the magnetic field shifting effect is achievable by comparing the shifted phase of the airgap flux density fundamental component waveforms. As can be seen, the magnetic fields of the both HPM asymmetric V-1 and U-1 IPMSMs are shifted about ~10 electrical degrees. A comparison of the open circuit linkage flux waveforms and spectra is given in Figure 10. As can be seen, the linkage flux waveforms of both machines are shifted whereas the maximum value of linkage flux in the HPM asymmetric U-1 IPMSM with 0.0663 Wb is higher than that of the HPM asymmetric V-1 IPMSM with 0.0573 Wb. Meanwhile, Figure 11a,b illustrates the open circuit back-EMF waveforms and spectra at 2100 r/min, respectively. As can be seen, the back-EMF's fundamental component of the HPM asymmetric U-1 IPMSM with 56.34 V is ~13% higher than that of the HPM asymmetric V-1 IPMSM with 49.7 V. Having a lower back-EMF may be considered as a safety measure especially at high speeds, when a fault can transfer a high voltage across the terminals of the inverter and cause damage.

Therefore, Figure 11c compares the variation of peak-to-peak values of open circuit back-EMFs in both machines. As can be seen, the peak-to-peak value of the HPM asymmetric V-1 IPMSM at 10 kr/min with 466.74 V is 47.92 V (~9.3%) less than that of the HPM asymmetric U-1 topology.

Figure 12a,b compares the variations of torques and *dq*-axis inductances with the current advancing angle at 625 A_{max} and 2100 r/min. As can be seen, although both machines have the same peak torque, their profiles of torque with current advancing angle are different.

Meanwhile, as the employed high energy product REPM (N28AH) has a residual flux density of 1.075 T, which is almost 2.3 times of that in the low coercive FEPM (TDK-FB13B) with 0.475 T, a concern regarding the irreversible demagnetisation of FEPM rises by the demagnetisation *d*-axis current and REPMs. This is because when the operating point of FEPM is pushed below the knee point, the capability of FEPM to produce the magnetic field will be permanently reduced. This can not only lead to a significant deterioration of the electromagnetic performances including torque, efficiency, etc., but also can reduce the service life of the PM machine in EV application. Therefore, it will increase the cost of repairs and reduce the confidence of the EV consumers. As a result, preventing the demagnetisation of FEPM acts as a crucial consideration during the design of PM machines for EV application. In addition, the difference in the magnetic properties of REPMs and FEPMs shows that, in contrast to REPMs, the FEPMs will be at a higher risk of irreversible demagnetisation at low temperature. Therefore, the demagnetisation withstand capability study of FEPMs needs to be conducted at low temperature, for example, −40°C. It is worth mentioning that the knee point of FEPM is selected as 0.06 T based on the magnetic flux density (B) versus the magnetic field strength (H) curve of TDK-FB13B at −40°C of temperature provided by the PM database within JMAG designer FEA software. This magnetic property can also be found online. Figure 13a–d compares the decomposed flux density distributions of FEPMs in their magnetisation direction in both machines at −40°C and open circuit condition. It is worth mentioning that in Figure 13a,b, the rotors are assumed to be out of stator, for example, during the assembling stage or maintenance. As can be seen, the FEPM2 suffers from regional self-demagnetised areas when rotor is outside of stator in both HPM asymmetric V-1 and U-1 IPMSMs. However, when the

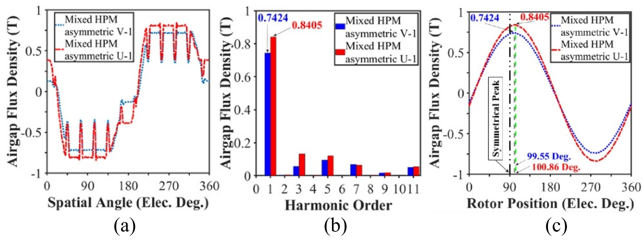

FIGURE 9 | Comparison of open circuit airgap flux densities of HPM asymmetric V-1 and U-1 IPMSMs. (a) Waveforms. (b) Spectra. (c) Fundamental component waveforms.

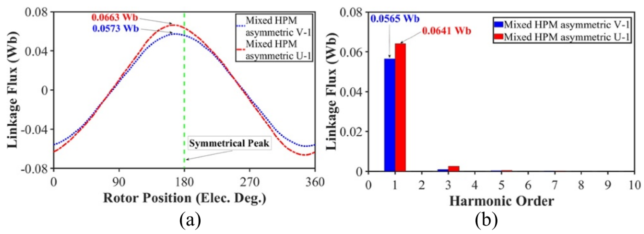

FIGURE 10 | Comparison of open circuit linkage fluxes in HPM asymmetric V-1 and U-1 IPMSMs. (a) Waveforms. (b) Spectra.

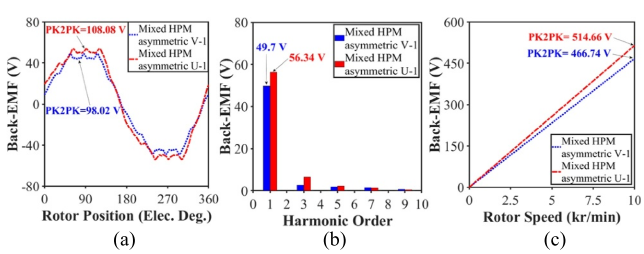

FIGURE 11 | Comparison of open circuit back-EMFs in HPM asymmetric V-1 and U-1 IPMSMs. (a) Waveforms. (b) Spectra. (c) Peak to peak values with speed.

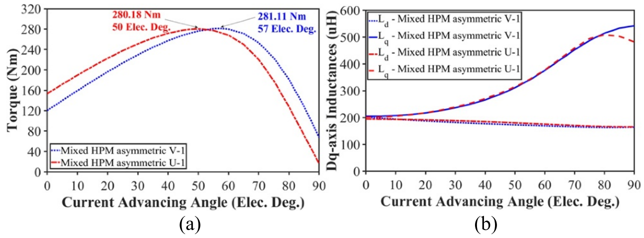

FIGURE 12 | Comparison of torque and *dq*-axis inductances with current advancing angle at 625 A_{max} and 2100 r/min in HPM asymmetric V-1 and U-1 IPMSMs. (a) Torques. (b) *Dq*-axis inductances.

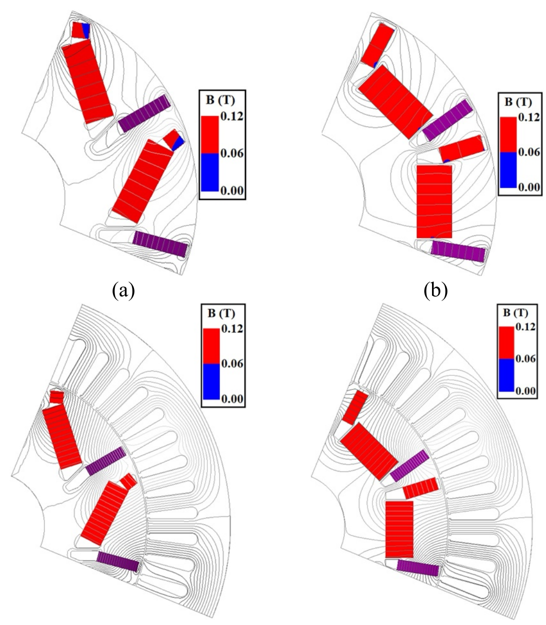

FIGURE 13 | Comparison of decomposed flux density distributions of FEPMs at −40°C and open circuit condition. (a) HPM asymmetric V-1 rotor (without stator). (b) HPM asymmetric U-1 rotor (without stator). (c) HPM asymmetric V-1 rotor (with stator). (d) HPM asymmetric U-1 rotor (with stator).

rotors are inside the stator as can be seen in Figure 13c,d, the PM fluxes find a lower reluctance in their magnetic path by circulating through the stator. As a result, no demagnetisation occurs at this condition. On the contrary, Figure 14 presents a demagnetisation withstand capability study of FEPMs in both machines at −40°C when the *d*-axis currents ranging from twice to triple of rated current are applied. As can be seen, the FEPM2 significantly suffers from the irreversible demagnetisation in both HPM asymmetric V-1 and U-1 IPMSMs. Therefore, the application of FEPMs in these positions should be prohibited to increase the demagnetisation withstand capabilities of the proposed HPM machines which may be at the cost of torque reduction. In this regard, Figure 15. Compares the produced torque by both HPM machines with and without FEPM2 at 625 A_{max} and 2100 r/min. As expected, by removing the FEPM2, the developed torques of the HPM asymmetric V-1 and U-1 IPMSMs drop for ~9.5 and ~14.9 Nm, respectively. Consequently, the modified topologies, for example, the final proposed HPM asymmetric V-2 and U-2 IPMSMs, are expected to use slightly more REPM volume to generate 280 Nm.

3.3 | Optimisation Results (HPM Asymmetric V-2 and U-2)

The optimisation results of the proposed HPM asymmetric V-2 and U-2 IPMSMs, which are modified to improve the demagnetisation withstand capability of FEPMs, are presented in this section. Figure 16a shows the parametric model of the HPM asymmetric V-2 IPMSM, whereas the optimisation result and the optimum cross section of this machine are presented in Figure 16b,c, respectively. As can be seen, this machine requires ~103.62 cm^3 volume of REPM (~31% less than baseline) to deliver 280 Nm peak torque at 625 A_{max} and 2100 r/min. Meanwhile, Figure 17a–c presents the parametric model, the optimisation result, and the optimum cross section of the HPM asymmetric U-2 IPMSM, respectively. As can be seen, to produce 280 Nm torque at 625 A_{max} and 2100 r/min, ~115.09 cm^3 volume of REPM (~23.4% less than baseline) is consumed in this

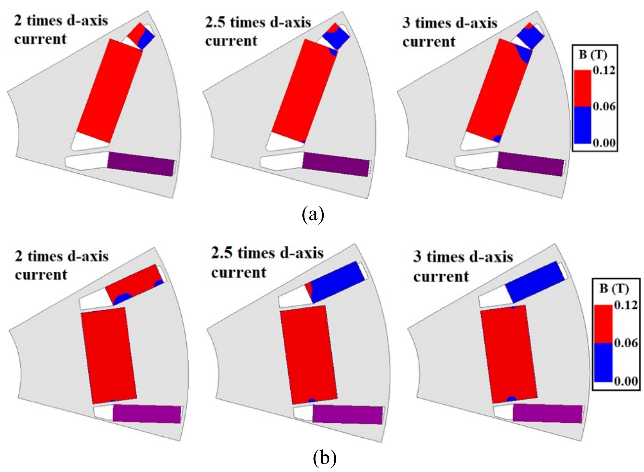

FIGURE 14 | Comparison of decomposed flux density distributions of FEPMs at −40°C when *d*-axis currents ranging from twice to triple rated current are applied. (a) HPM asymmetric V-1 IPMSM. (b) HPM asymmetric U-1 IPMSM.

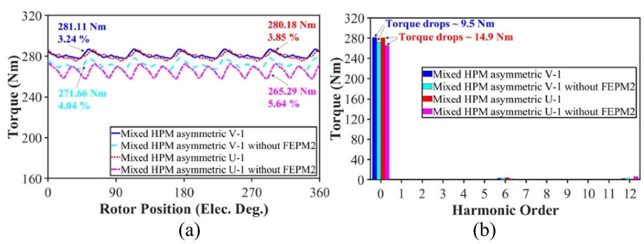

FIGURE 15 | Comparison of torque waveforms and spectra at 625 A_{max} and 2100 r/min in both HPM asymmetric V-1 and U-1 IPMSMs considering the effect of FEPM2 removal. (a) Waveforms. (b) Spectra.

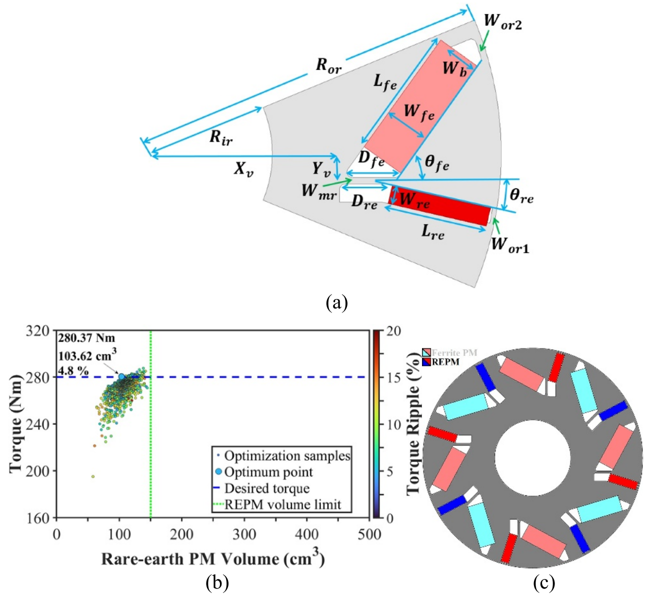

FIGURE 16 | HPM asymmetric V-2 IPMSM. (a) Parametric model. (b) Optimisation result at 625 A_{max} and 2100 r/min. (c) Optimum cross section.

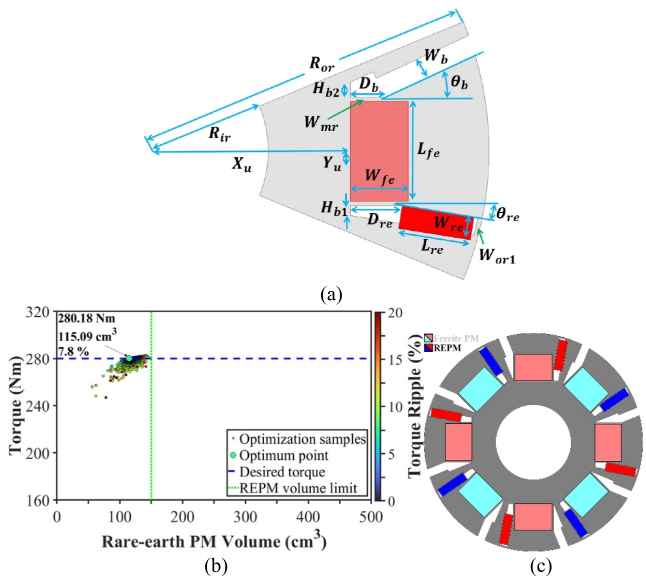

FIGURE 17 | HPM asymmetric U-2 IPMSM. (a) Parametric model. (b) Optimisation result at 625 A_{max} and 2100 r/min. (c) Optimum cross section.

structure. Consequently, compared to those of the HPM asymmetric V-1 and U-1 IPMSMs, the saved volumes of REPM in the proposed HPM asymmetric V-2 and U-2 IPMSMs are reduced from 42% to 31%, and from 40.5% to 23.4%, respectively. However, as will be shown later, the demagnetisation withstand capability of FEPM is considerably improved in both proposed HPM machines. The definitions of the design parameters and their optimum values are summarised in Table 3.

Figure 18a–c presents a comparison of the von-mises stress distributions of the proposed HPM asymmetric V-2 and U-2 IPMSMs to that of the baseline at 10 kr/min when the frictional contacts with the friction coefficient of 0.2 are used.

It should be noted that the same widths of the ribs as the HPM asymmetric V-1 and U-1 IPMSMs are employed for the sake of comparison. As can be seen, the proposed HPM machines benefit from a lower maximum stress on the ribs compared to the baseline. In the proposed HPM asymmetric V-2 IPMSM, the movements of the REPM and FEPM1 are well controlled with the introduced verges. Meanwhile, by removing the FEPM2 (also means the less contact regions between PMs and core), less force is transferred to the second outer rib. Consequently, the maximum stress on this rib is reduced from ~236 to ~205 MPa (−13%). Similarly, the centrifugal force in the HPM asymmetric U-2 IPMSM is also controlled with the introduced verge and reduced contact regions. As a result, although the volume of PMs is increased, the maximum von-mises stress on the ribs remained almost unchanged. Consequently, the proposed HPM asymmetric V-2 and U-2 IPMSMs and the baseline can provide the safety factors of 2.2, 2 and 1.9, respectively.

3.4 | Comparison of HPM Asymmetric V-2 and U-2 IPMSMs With Baseline

The open circuit flux density and flux line distributions of the baseline and the proposed HPM asymmetric V-2 and U-2 IPMSMs are shown in Figure 19. As can be seen, the *d*-axis of the proposed HPM asymmetric machines is shifted compared to that of the baseline. Moreover, the comparison of the open circuit airgap flux density waveforms, spectra, and fundamental component variations with rotor position are presented in Figure 20. By comparing the shifted phase of the airgap flux density fundamental component waveforms in Figure 20c, it is revealed that the HPM asymmetric U-2 IPMSM has the highest shifted *d*-axis by ~22.6 electrical degrees which is twice of that in the HPM asymmetric V-2 IPMSM. Figure 21 presents a comparison of the open circuit flux linkage waveforms and spectra. As can be seen, unlike the baseline, the flux linkage waveforms of the proposed HPM asymmetric machines are shifted. In addition, the amplitudes of the fundamental components of the baseline and HPM asymmetric V-2 and U-2 IPMSMs are 0.0663 Wb, 0.0525 Wb, and 0.0566 Wb, respectively.

The open circuit back-EMF waveforms and spectra at 2100 r/min are compared in Figure 22. As can be seen, the back-EMF's fundamental component of the baseline with 58.3 V is higher than those of the HPM asymmetric V-2 and U-2 IPMSMs with 46.2 and 49.8 V, respectively. Meanwhile, Figure 22c compares

TABLE 3 | Design parameters of HPM asymmetric V-2 and U-2 IPMSMs.

Parameter	HPM asymmetric V-2	HPM asymmetric U-2
Rotor outer radius (R_{or})—mm	65	
Rotor inner radius (R_{ir})—mm	22.5	
V-shape centre in *x*-axis (X_v)—mm	36.19	—
V-shape centre in *y*-axis (Y_v)—mm	8.17	—
U-shape centre in *X*-axis (X_u)—mm	—	36.62
U-shape centre in *Y*-axis (Y_u)—mm	—	0.114
Width of REPM (W_{re})—mm	4.96	5.25
Length of REPM (L_{re})—mm	17.28	18.15
Width of FEPM (W_{fe})—mm	9.52	15.79
Length of FEPM (L_{fe})—mm	25.2	22.14
Width of barrier (W_b)—mm	6.48	5.04
Angle of REPM (θ_{re})—Degree	17.34	10.52
Angle of FEPM (θ_{fe})—Degree	61.65	—
Angle of barrier (θ_b)—Degree	—	22.11
REPM displacement (D_{re})—mm	8.75	6.79
FEPM displacement (D_{fe})—mm	9.93	—
Barrier displacement (D_b)—mm	—	16.16
Height of barrier 1 (H_{b1})—mm	—	2.77
Height of barrier 2 (H_{b2})—mm	—	0.29
Width of middle rib (W_{mr})—mm	1.2	0.8
Width of outer rib 1 (W_{or1})—mm	0.8	0.8
Width of outer rib 2 (W_{or2})—mm	1.2	—

the variations of open circuit back-EMFs with speed. As can be seen, the peak-to-peak values of the both HPM asymmetric V-2 and U-2 IPMSMs at 10 kr/min are about 440 V which are ~18.8%

less than that of the baseline with 542 V. Therefore, the proposed HPM asymmetric V-2 and U-2 IPMSMs are expected to be safer than the baseline at high speeds in terms of having a lower back-EMF across the terminals of the inverter if a fault occurs. This is while, the harmonics of the proposed HPM asymmetric V-2 IPMSM is slightly lower than those of the other HPM counterpart with U-shape structure. Finally, Figure 23 compares cogging torque waveforms and spectra of these three machines at open circuit condition. As can be seen, the HPM asymmetric V-2 IPMSM benefits from the lowest cogging torque.

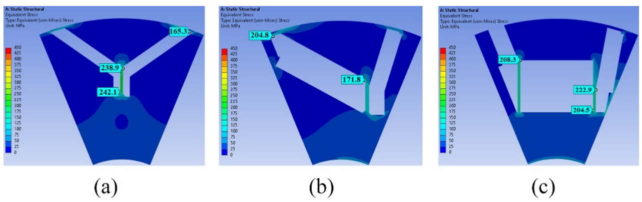

FIGURE 18 | Comparison of von-mises stress distributions at 10 kr/min. (a) REPM-based symmetrical V IPMSM. (b) HPM asymmetric V-2 IPMSM. (c) HPM asymmetric U-2 IPMSM.

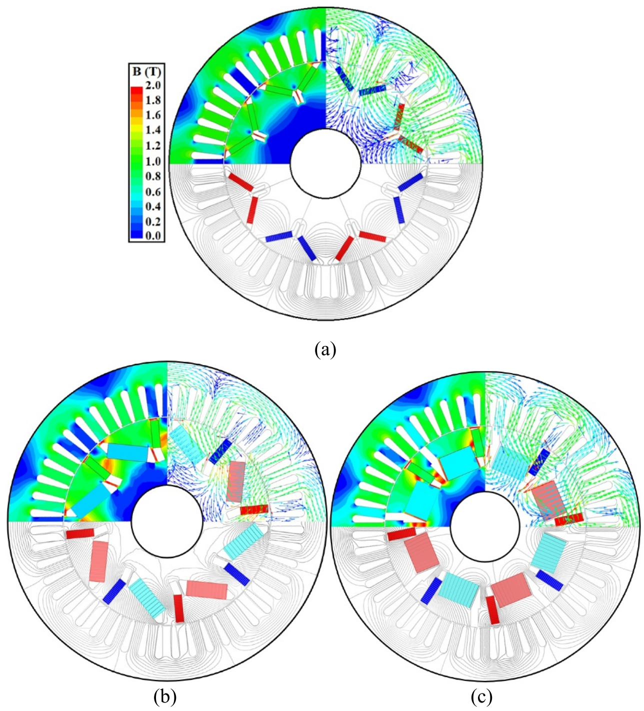

FIGURE 19 | Comparison of open circuit flux density and flux line distributions. (a) REPM-based symmetrical V IPMSM (baseline). (b) HPM asymmetric V-2 IPMSM. (c) HPM asymmetric U-2 IPMSM.

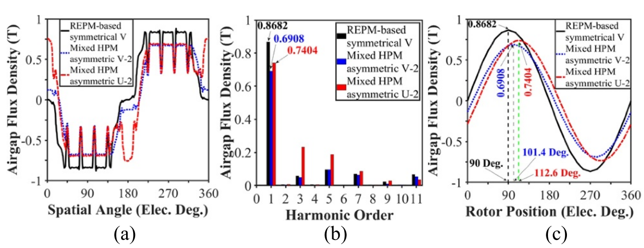

FIGURE 20 | Comparison of open circuit airgap flux densities of baseline and HPM asymmetric V-2 and U-2 IPMSMs. (a) Waveforms. (b) Spectra. (c) Fundamental component waveforms.

Figure 24 compares the peak torque waveforms and spectra at 625 A_{max} and 2100 r/min. As these machines are optimised to deliver the same peak torque, a similar performance is expected. Moreover, Figure 25a,b compare the variations of torques and *dq*-axis inductances with the current advancing angle at 625 A_{max} and 2100 r/min. As can be seen in Figure 25a, the variations of torque with current advancing angle are different which suggests that these machines would have different reluctance torque and PM torque components. Meanwhile, as can be seen in Figure 25b, the

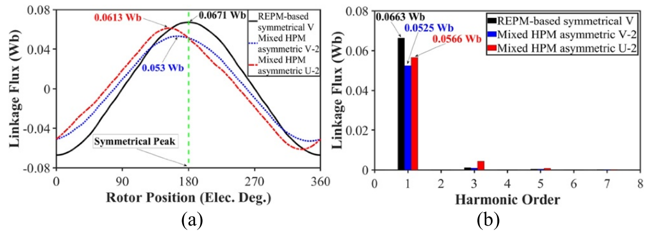

FIGURE 21 | Comparison of open circuit flux linkages of baseline and HPM asymmetric V-2 and U-2 IPMSMs. (a) Waveforms. (b) Spectra.

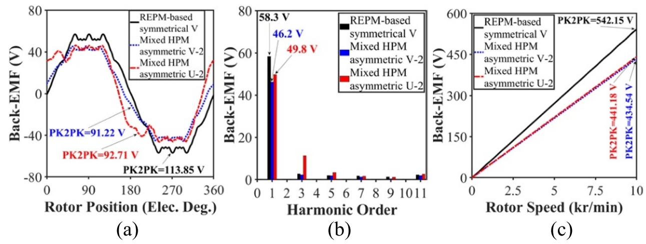

FIGURE 22 | Comparison of open circuit back-EMFs of baseline, and HPM asymmetric V-2 and U-2 IPMSMs. (a) Waveforms. (b) Spectra. (c) Peak to peak values with speed.

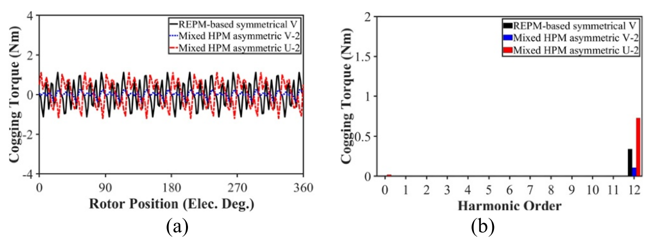

FIGURE 23 | Comparison of open circuit cogging torques of baseline and HPM asymmetric V-2 and U-2 IPMSMs. (a) Waveforms. (b) Spectra.

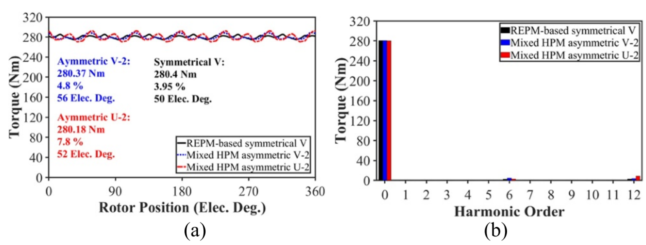

FIGURE 24 | Comparison of torque waveforms and spectra of baseline, and HPM asymmetric V-2 and U-2 IPMSMs at 625 A_{max} and 2100 r/min. (a) Waveforms. (b) Spectra.

q-axis inductances of the proposed HPM asymmetric IPMSMs are slightly lower than that of the baseline. This is because the REPM is rotated towards the centre of the pole in the optimum designs of these topologies as shown in Figures 16c and 17c. Therefore, the cross sections of the q-axis flux path are reduced which results in an increased saturation leading to a reduced q-axis inductance. Meanwhile, the d-axis inductances of the proposed machines are lower than that of the baseline due to having thicker flux barriers in d-axis. Therefore, the higher reluctance torque components are expected in the proposed HPM asymmetric V-2 and U-2 IPMSMs compared to that of the baseline. For a precise decomposition of torque components, the frozen permeability method is used at 625 A_{max} and 2100 r/min in Figure 26 where the optimum current advancing angles of each machine are employed based on the results of Figure 25a. As can be seen, the reluctance torques of the proposed HPM asymmetric V-2 and U-2 IPMSMs are ~10 and ~12 Nm more than that of the baseline with 198.75 Nm, respectively. Therefore, for the same total torque, these machines would only need ~70 Nm of PM torque. Meanwhile, considering the FEPM torque contribution, the proposed HPM asymmetric V-2 and U-2 IPMSMs would only require 43.5 and 45 Nm of REPM torque components which are ~38 and ~37 Nm less than that of the baseline, respectively. As a result, the volume of REPM can be effectively reduced at no torque deterioration.

Figure 27a,b compares the torque/power-speed characteristics at 625 A_{max}. As these machines are designed for the same torque at low speed when 625 A_{max} and 2100 r/min are applied, these characteristics are expected to be the same at constant torque region. However, as the open circuit performances of these machines are different, they are expected to reach the DC link voltage limit at different speeds and have different torque/power-speed characteristics at the flux weakening region. Meanwhile, the commercialised IPMSM has a maximum power cap of 80 kW [28] which is also applied to these three machines.

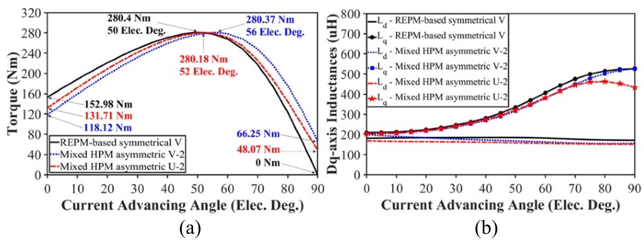

FIGURE 25 | Comparison of torques and dq-axis inductances of baseline and HPM asymmetric V-2 and U-2 IPMSMs at 625 A_{max} and 2100 r/min. (a) Torques. (b) Dq-axis inductances.

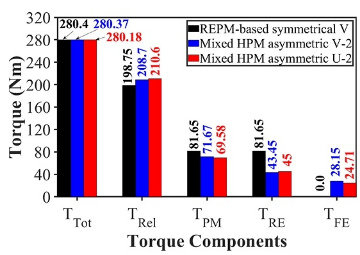

FIGURE 26 | Comparison of decomposed torque components of baseline and HPM asymmetric V-2 and U-2 IPMSMs using frozen permeability method at 625 A_{max} and 2100 r/min.

Therefore, the torque/power-speed characteristics of these machines at flux weaking region become the same, that is, constant power region.

In general, the constant power speed range (CPSR) capability under the flux weakening condition is an important feature in PM machines for the high speed applications, for example, EV.

This feature can be estimated by comparing the amplitude of the phase current (I_s) and the characteristic current (I_{ch}) which is definable as follows:

$$I_{ch} = \frac{\Psi_{pm}}{L_d}. \tag{8}$$

Whereas a closer armature current to the characteristic current, a higher CPSR capability under the flux weakening condition [29]. Therefore, using the results of Figures 21a and 25b, the characteristic currents of these machines are calculated as listed in Table 4. As can be seen, the proposed HPM asymmetric V-2 IPMSM benefits from a better CPSR capability than the other machines.

Meanwhile, the flux weakening capability can be defined by the flux weakening ratio (ξ) using the equation given below:

$$\xi = \frac{I_d}{I_{ch}}. \tag{9}$$

Whereas a higher flux weakening ratio approaching 1, a better flux weakening capability [30]. It can be concluded that at the

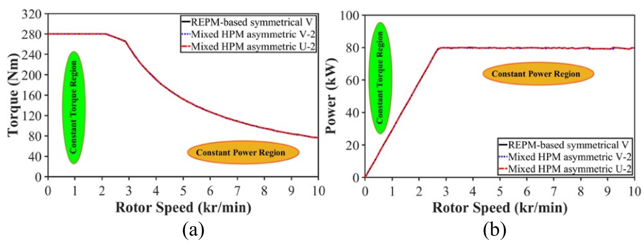

FIGURE 27 | Comparisons of torque-speed and power-speed characteristics at 625 A_{max}. (a) Torque-speed characteristics. (b) Power-speed characteristics.

TABLE 4 | Comparison of CPSR and flux weakening capabilities.

Parameter	Baseline	HPM asymmetric V-2	HPM asymmetric U-2
Rated phase current (A)		312.5	
PM flux linkage (Wb)	0.0671	0.053	0.0613
D-axis inductance (mH)	0.1846	0.1652	0.158
Characteristic current (A)	363.5	320.8	388
Flux weakening ratio	0.575	0.724	0.559

same d-axis current, a lower characteristic current leads to a higher flux weakening capability. Meanwhile, from Figure 25a, it is expected that the proposed HPM asymmetric V-2 IPMSM employs a higher d-axis current which results in even a higher flux weakening ratio as presented in Table 4. Therefore, without a power cap at flux weakening region, the proposed HPM asymmetric V-2 IPMSM is expected to benefit from a better performance than the other topologies.

The efficiency (η) of these PM machines can be obtained by the following:

$$\eta = \frac{P_{\text{out}}}{P_{\text{out}} + P_{\text{cu}} + P_{\text{core}} + P_{\text{mec}}} \times 100, \tag{10}$$

where P_{out}, P_{cu}, P_{core}, and P_{mec} are the output power, the copper loss, the iron loss, and the mechanical loss, respectively.

The mechanical loss calculation requires two coefficients as follows which are taken from [31]:

$$P_{\text{mec}} = k_{\text{mec1}} f + k_{\text{mec2}} f^2, \tag{11}$$

where f is the frequency, and k_{mec1} and k_{mec2} are the mechanical loss coefficients.

By sharing the same stator, stack length, and winding configurations, the copper losses of these machines are expected to be almost the same as shown in Figure 28a. However, the FEA results in Figure 28b shows that the iron loss of the HPM asymmetric U-2 IPMSM is higher than that of the others due to having higher harmonic components of the airgap flux density as shown in Figure 20b. Finally, as can be seen in Figure 28c, the efficiencies of the baseline and the proposed HPM asymmetric V-2 and U-2 IPMSMs can exceed 97%. Meanwhile, this region in the HPM asymmetric U-2 IPMSM is smaller than the others due to the increased iron loss.

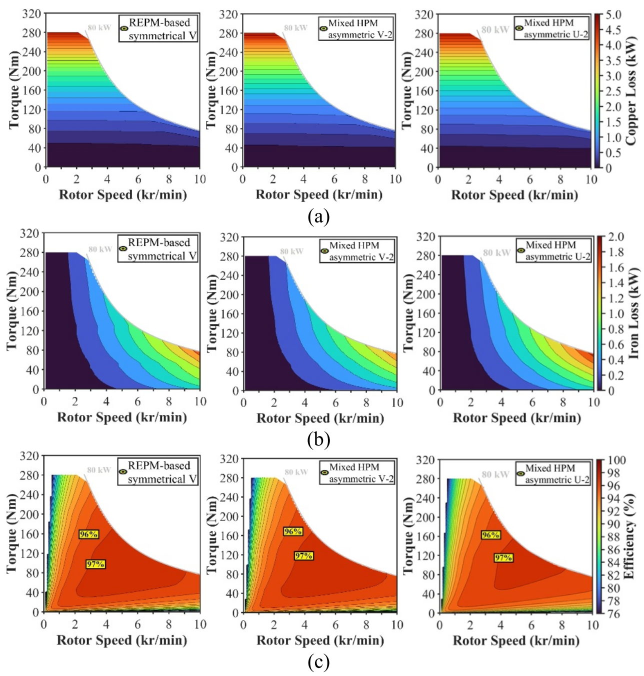

FIGURE 28 | Comparisons of copper loss, iron loss, and efficiency maps of these three machines. (a) Copper loss maps. (b) Iron loss maps. (c) Efficiency maps.

Figure 29a–d compares the decomposed flux density distributions of FEPMs in their magnetisation direction in the proposed HPM asymmetric V-2 and U-2 IPMSMs at −40°C and open circuit condition. As can be seen, no demagnetised region can be found in both machines when the rotor is either outside or inside of the stator. Meanwhile, a similar investigation under the overload conditions, when the d-axis currents ranging from twice to triple of the rated current are applied at −40°C, is presented in Figure 30. As can be seen, the demagnetised

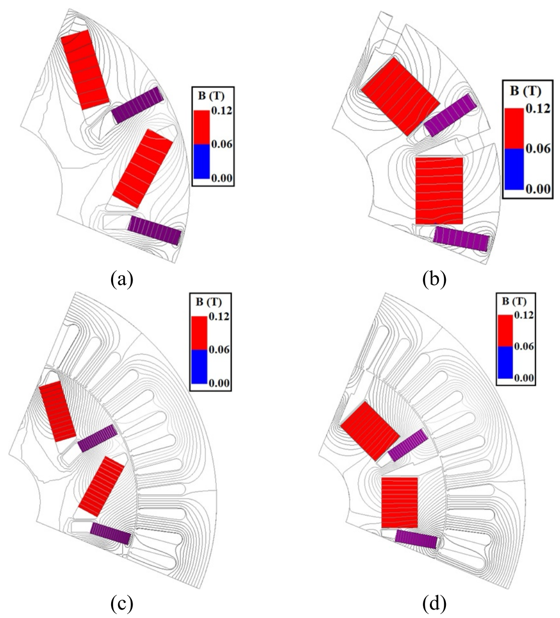

FIGURE 29 | Comparison of decomposed flux density distributions of FEPMs at −40°C and open circuit condition. (a) HPM asymmetric V-2 rotor (without stator). (b) HPM asymmetric U-2 rotor (without stator). (c) HPM asymmetric V-2 rotor (with stator). (d) HPM asymmetric U-2 rotor (with stator).

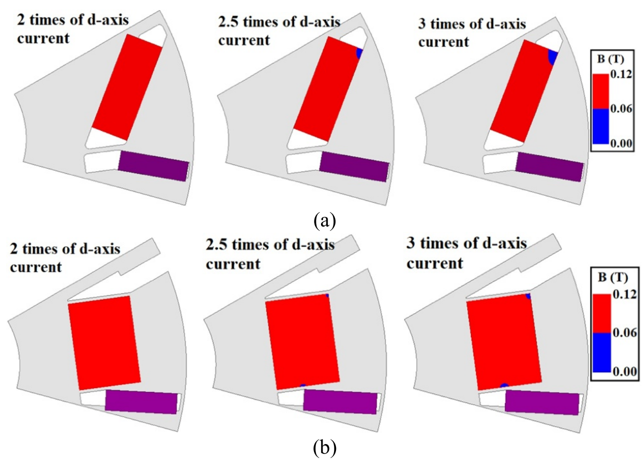

FIGURE 30 | Comparison of decomposed flux density distributions of FEPMs at −40°C when d-axis currents ranging from twice to triple rated current are applied. (a) HPM asymmetric V-2 IPMSM. (b) HPM asymmetric U-2 IPMSM.

regions of FEPMs are significantly reduced compared to those of the HPM asymmetric V-1 and U-1 IPMSMs in Figure 14.

Finally, Figure 31 compares the decomposed flux density distribution of REPMs at 120°C and triple of rated d-axis current. As can be seen, only a negligible area of REPMs is at the risk of irreversible demagnetisation at this condition.

4 | Comparison of PM Cost

To improve the torque with REPM volume ratio, all investigated HPM asymmetric IPMSMs in this paper are optimised to deliver the same torque at a lower volume of REPM consumption. Therefore, despite the comparison of performances including electromagnetic, mechanical, and demagnetisation withstand capability, a comparison of PM cost can emphasise the advantages of the proposed HPM asymmetric machines. As a result, Table 5 presents a detailed comparison of the volumes of both PMs and the PM cost estimations in p.u. when those of the baseline topology are considered as reference. These estimations are first calculated using the general assumption of REPM to FEPM cost ratio of 10. Meanwhile, the historical price chart of REPMs show two significant price surges in 2011 and 2021 which implies that the PMs cost ratio of 10 cannot be guaranteed in all times. Therefore, the REPM to FEPM cost ratio of 30 [17] is also included to consider the future rare-earth price fluctuations.

As can be seen, compared to the baseline at the same torque of 280 Nm, the required volumes of REPM in the proposed HPM asymmetric V-2 and U-2 IPMSMs are reduced by ~31% and ~23.4%, respectively. These savings are higher in the HPM asymmetric V-1 and U-1 IPMSMs, where the demagnetisation withstand capability of FEPMs are not considered. The required volumes of REPM in these machines are reduced by ~42% and ~40.5%, respectively. Meanwhile, considering the price of REPM being 10 times the FEPM, the PM cost reductions of the proposed HPM asymmetric V-2 and U-2 IPMSMs are ~18% and ~5%, respectively. Obviously, if the price of REPM increases in future, for example, REPM to FEPM cost ratio of 30, the reduced amount of the PM cost will be increased to ~27% and ~17%, respectively. Finally, not only the ratios of torque per REPM volume in all HPM machines are higher than that of the baseline, but also the ratios of torque per rotor active mass of these machines are higher. This is mainly due to using a high volume of FEPMs with low mass density.

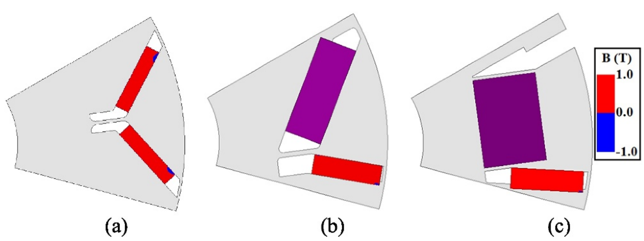

FIGURE 31 | Comparison of decomposed flux density distributions of REPMs at 120°C and triple of rated d-axis current. (a) REPM-based symmetrical V IPMSM. (b) HPM asymmetric V-2 IPMSM. (c) HPM asymmetric U-2 IPMSM.

In Ref. [32], the total manufacturing cost of a PM machine for EV application is divided into seven components including material, purchased parts, equity, maintenance, tools and area, labour, and assembly. Whereas 'material' stands for the cost of PMs, copper, etc., 'purchased parts' represents the cost of bearings, cooling pump, etc., 'equity' is the cost of the production line investment, 'maintenance' is the cost of maintaining the production line, and 'tools and area' is the cost of tools and the occupied area with these tools. In addition, 'labour' and 'assembly' are the costs of human labour and final assembly of all components, respectively. It is shown that producing a PM machine in high production volumes can reduce the total cost of a PM machine unit by up to 77% compared to that of the low production volumes. This is mainly due to the reduction of costs in equity, tools and area, and maintenance sections. Meanwhile, for the high production volumes over 100k units per year, the cost of material becomes the most expensive section which can form about more than half of

TABLE 5 | Comparison of PMs' volume, mass, and cost estimation.

		HPM asymmetric IPMSMs			
	Baseline	V-1	U-1	V-2	U-2
Total torque (Nm)	280.4	281.11	280.18	280.37	280.18
Volume of REPM (cm^3)	150.21	87.3	89.28	103.62	115.09
Volume of FEPM (cm^3)	—	320.32	404.41	289.67	422.22
Mass of REPM (kg)	1.142	0.663	0.679	0.788	0.875
Mass of FEPM (kg)	0.0	1.602	2.022	1.448	2.111
Volume of rotor electrical steel (cm^3)	1536.2	1253.5	1206.3	1248.8	1066.6
Mass of rotor electrical steel (kg)	11.752	9.589	9.228	9.553	8.159
Total mass of rotor active parts (kg)	12.894	11.854	11.929	11.789	11.145
Total torque per rotor active mass (Nm/kg)	21.75	23.71	23.49	23.78	25.14
Total torque per REPM volume (Nm/cm^3)	1.867	3.220	3.138	2.706	2.434
REPM volume reduction (%)	0	−41.88	−40.56	−31.02	−23.38
PM cost estimation (p.u.)*	1	0.72	0.77	0.82	0.95
PM cost estimation (p.u.)**	1	0.63	0.65	0.73	0.83

Note: Mass densities of REPM, FEPM, and rotor electrical steel are 7.6 g/cm^3, 5 g/cm^3 and 7.65 g/cm^3, respectively. REPM to FEPM cost ratios: *10, **30.

the total cost of the PM machine. Consequently, reducing the cost of PMs would be even more attractive for the mass production volumes of IPMSMs with the aim of producing more cost-effective commercialised EVs in future.

5 | Experimental Validation

To validate the FEA results, two small laboratory size prototypes with 24-slot/8-pole (24s8p) HPM asymmetric V- and U-shape arrangements of PMs are manufactured as shown in Figure 32. These machines are optimised to deliver 2 Nm torque at lower volume of REPM with the copper loss constraint of 40 W and the same dimensional parameters as listed in Table 6. Then, they are tested using the dynamic and static test benches as presented in Figure 33. The dynamic platform is used to measure the back-EMF and the transient torque, and the static test bench is employed to measure the cogging torque and the static torque [33]. The volumes of REPM and FEPM are compared in Table 7. As can be seen at the same size and performance, the HPM asymmetric V-shape prototype requires 8.16 cm^3 volume of REPM which is ~8.5% less than that of the HPM asymmetric U-shape prototype with 8.92 cm^3. This agrees with the conclusion of PM volume comparison in Table 5.

Figures 34 and 35 compare the open-circuit FEA predicted and measured back-EMFs at 250 r/min and cogging torques, respectively. As can be seen in Figure 34, the back-EMF of the HPM asymmetric U-shape prototype is slightly higher than that of the V-shape counterpart and matches with Figure 22. In addition, the cogging torque of the HPM asymmetric V-shape IPMSM is negligible which was expected and matches with the cogging torque comparison in Figure 23.

Figure 36 compares the variations of static torques with rotor position, when DC current ($I_a = -2I_b = -2I_c = I_{DC}$) is injected into the windings. Meanwhile, Figures 37 and 38 present the

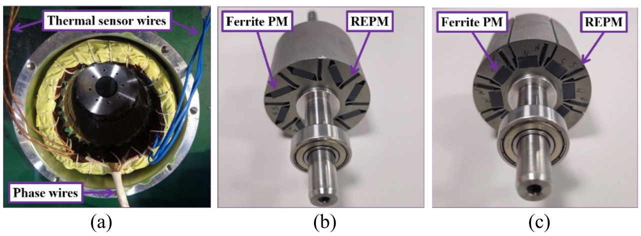

FIGURE 32 | Prototypes. (a) Shared stator. (b) HPM asymmetric V rotor. (c) HPM asymmetric U rotor.

TABLE 6 | Main dimensional parameters for both prototypes.

Parameters	Values	Parameters	Values
Stator outer diameter	100 mm	Slot number	24
Stator inner diameter	63 mm	Pole number	8
Active stack length	50 mm	Turns per coil	60
Airgap length	1 mm	Phase resistance	1.6 Ω
Remanence of N28AH	1.075 T	Phase current	4 A_{max}
Remanence of TDK-FB13B	0.475 T		

TABLE 7 | Volume of PMs in both prototypes.

PM type	HPM asymmetric V-shape prototype	HPM asymmetric U-shape prototype
REPM (cm^3)	8.16	8.92
FEPM (cm^3)	20.9	23.3

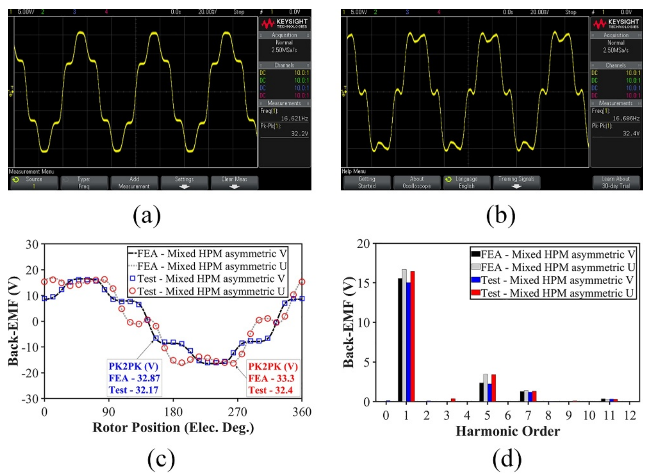

FIGURE 34 | FEA predicted and measured line back-EMFs at open circuit and 250 r/min. (a) Experimental waveform of HPM asymmetric V-shape prototype. (b) Experimental waveform of HPM asymmetric V-shape prototype. (c) Comparison of waveforms. (d) Comparison of spectra.

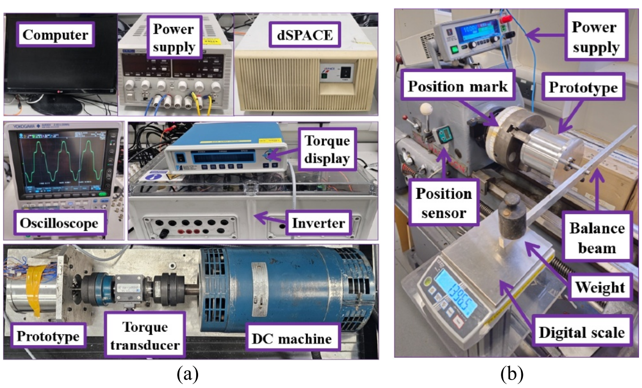

FIGURE 33 | Experimental test benches. (a) Dynamic test rig. (b) Static test rig.

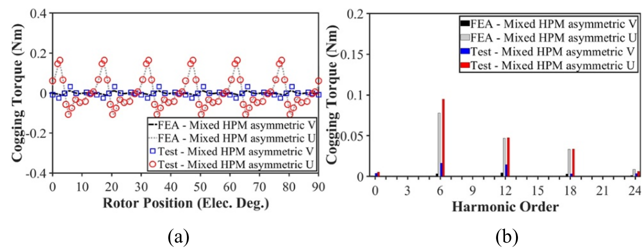

FIGURE 35 | FEA predicted and measured cogging torques at open circuit. (a) Waveforms. (b) Spectra.

variations of predicted and measured average torques with current amplitude at optimum current advancing angles and 250 r/min, and with current advancing angle at 4 A_{max} and 250 r/min, respectively. As can be seen, both machines can produce the required torque with a good agreement accounting for ~6% error. In addition, the difference in the optimum current advancing angles matches with the results of Figure 25a. Finally, Figure 39 compares the measured waveforms of torques and three phase currents at 250 r/min.

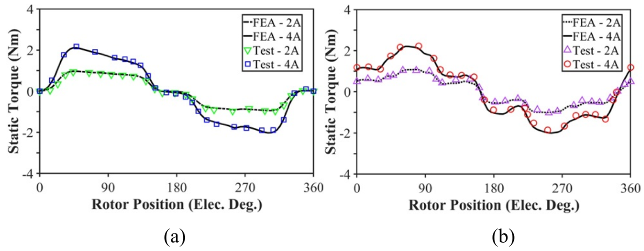

FIGURE 36 | FEA predicted and measured static torques at different DC currents. (a) HPM asymmetric V-shape prototype. (b) HPM asymmetric U-shape prototype.

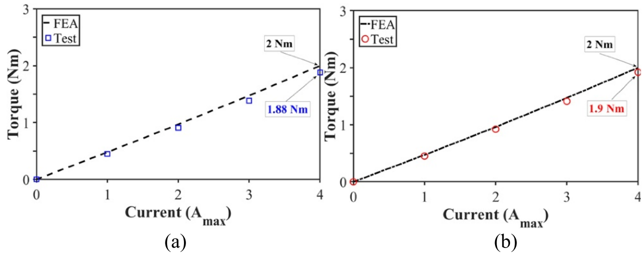

FIGURE 37 | Variation of FEA predicted and measured average torques with current amplitude at 250 r/min. (a) HPM asymmetric V-shape prototype. (b) HPM asymmetric U-shape prototype.

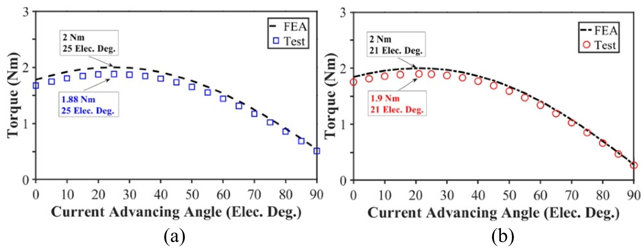

FIGURE 38 | Variation of FEA predicted and measured average torques with current advancing angle at 4 A_{max} and 250 r/min. (a) HPM asymmetric V-shape prototype. (b) HPM asymmetric U-shape prototype.

FIGURE 39 | Measured torque waveforms at 4 A_{max} and 250 r/min. (a) HPM asymmetric V-shape prototype. (b) HPM asymmetric U-shape prototype.

As can be seen, the peak to peak value of the measured torques in asymmetric HPM V-shape and U-shape IPMSMs are ~0.18 and ~0.25 Nm which are slightly higher than those of the FEA results with ~0.15 and ~0.18 Nm, respectively. The simulation results show that using the DC-link voltage of 150 V, the maximum efficiencies of both prototypes can exceed ~90% at ~2700 r/min. Meanwhile, due to the lab limitations, the FEA predicted and measured efficiencies at three operating points are compared when the DC link voltage and maximum test speed are set as 65 V and 1000 r/min as shown in Table 8. As expected from the FEA results in Figure 28c, both machines have a similar efficiency in low speed regions.

6 | Conclusion

This paper proposes two novel HPM asymmetric V-2 and U-2 IPMSMs with high FEPM torque contribution accounting for a higher demagnetisation withstand capability of this magnet. First, two HPM asymmetric V-1 and U-1 IPMSMs are designed to effectively utilise the magnetic field shifting effect and the FEPM utilisation when the demagnetisation withstand capability was not considered. It is shown that compared to a REPM-based symmetrical V-shape IPMSM, these machines could have saved the required volume of REPM by 42% and ~40.5%, respectively. Meanwhile, it is also shown that the FEPMs in some locations are at a high risk of irreversible demagnetisation under both open circuit and overload conditions at −40°C. To address this issue, the employed FEPMs in the prohibited areas which were subject to the demagnetisation risk are removed by modifying the parametric models. Consequently, the HPM asymmetric V-2 and U-2 IPMSMs are proposed. Although the demagnetisation withstand capability of FEPMs is considerably increased, the percentages of the REPM volume reduction have decreased to ~31% and ~23.4%, respectively. This can be interpreted as the reduction of total PM cost by ~18% and ~5%, respectively, when the price of REPM being 10 times the FEPM. However, considering the future rare-earth price fluctuations by assuming the REPM to FEPM price ratio of 30, the total PM cost in these machines can be reduced by ~27% and ~17%, respectively.

In conclusion, the proposed HPM asymmetric V-2 IPMSM benefits from a lower volume of REPM and total PM cost along

TABLE 8 | FEA Predicted and measured efficiencies at 65 V DC link voltage.

	Condition	Efficiency (%)	
	Current (A), speed (r/min)	HPM asymmetric V-shape IPMSM	HPM asymmetric U-shape IPMSM
FEA	3, 750	80.23	80.22
Test		79.41	79.48
FEA	2, 1000	83.64	83.56
Test		82.89	82.92
FEA	1, 1000	81.42	81.22
Test		80.59	80.34

with lower harmonic components and a higher efficiency than that of the HPM asymmetric U-2 IPMSM. Meanwhile, the latter topology benefits from a higher magnetic field shifting effect and slightly better demagnetisation withstand capability of FEPMs. Finally, two small laboratory size prototypes of these machines are built and tested to verify the FEA results.

It is worth mentioning that the change of flux density distributions caused by the variations of PMs' properties at different rotor temperatures can result in different L_d and L_q, flux linkage, efficiency, etc., even at the same operating point. Therefore, a look up table for inverters may be required to include the rotor temperature when designing the HPM machines. This challenge will be investigated in future.

Author Contributions

Seyedmilad Kazemisangdehi: conceptualization, formal analysis, investigation, methodology, validation, writing – original draft. **Zi Qiang Zhu:** conceptualization, funding acquisition, methodology, project administration, resources, software, supervision, writing – review and editing. **Liang Chen:** resources, supervision, writing – original draft. **Lei Yang:** resources, supervision, writing – review and editing. **Yanjian Zhou:** resources, supervision, writing – review and editing.

Conflicts of Interest

This article was submitted to the special issue 'Reducing Rare Earth Permanent Magnet Content in Electric Machines for Transportation Applications: Advances and Design Challenges', for which the author—Z.i.Q.iang Zhu—is a Guest Editor. This article was not handled by the Guest Editorial team in the review process and was instead handled by one of the journal's Associate Editors. The Editor-in-Chief was not involved in the handling of the article or its peer review process. The Deputy Editor-in-Chief and handling Associate Editor have taken full responsibility of the editorial process for the article.The authors declare no conflicts of interest.

Data Availability Statement

Data available on request from the authors.

References

1. Z. Q. Zhu and D. Howe, "Electrical Machines and Drives for Electric, Hybrid, and Fuel Cell Vehicles," *Proceedings of the IEEE* 95, no. 4 (2007): 746–765, https://doi.org/10.1109/jproc.2006.892482.

2. L. Shao, A. E. H. Karci, D. Tavernini, A. Sorniotti, and M. Cheng, "Design Approaches and Control Strategies for Energy-Efficient Electric Machines for Electric Vehicles—A Review," *IEEE Access* 8 (2020): 116900–116913, https://doi.org/10.1109/access.2020.2993235.

3. U.S. D. o. Energy, "Advanced Vehicle Technologies Research Funding Opportunity Announcement," [Online], https://www.energy.gov/eere/vehicles/funding-opportunities.

4. B. Poudel, E. Amiri, P. Rastgoufard, and B. Mirafzal, "Toward Less Rare-Earth Permanent Magnet in Electric Machines: A Review," *IEEE Transactions on Magnetics* 57, no. 9 (2021): 1–19, https://doi.org/10.1109/tmag.2021.3095615.

5. Z. Q. Zhu and Y. Xiao, "Novel Magnetic-Field-Shifting Techniques in Asymmetric Rotor Pole Interior PM Machines With Enhanced Torque Density," *IEEE Transactions on Magnetics* 58, no. 2 (2021): 1–10, https://doi.org/10.1109/tmag.2021.3076418.

6. J. T. Chen and Z. Q. Zhu, "A Synchronous Permanent Magnet Machine," Siemens Gamesa Renewable Energy A/S, European Patent Application Number 11162813.7, filed 2011-04-18, EP2515417-B1, granted 2014-04-02.

7. Y. Xiao, Z. Q. Zhu, S. S. Wang, et al., "A Novel Asymmetric Interior Permanent Magnet Machine for Electric Vehicles," *IEEE Transactions on Energy Conversion* 36, no. 3 (2021): 2404–2415, https://doi.org/10.1109/tec.2021.3055260.

8. Y. Xiao, Z. Q. Zhu, G. W. Jewell, J. T. Chen, D. Wu, and L. M. Gong, "Influence of Armature Reaction on Magnetic-Field-Shifting Effect in Asymmetric Interior Permanent Magnet Machines," *IEEE Transactions on Energy Conversion* 37, no. 2 (2021): 1475–1488, https://doi.org/10.1109/tec.2021.3132588.

9. Y. Shen and Z. Q. Zhu, "Analysis of Electromagnetic Performance of Halbach PM Brushless Machines Having Mixed Grade and Unequal Height of Magnets," *IEEE Transactions on Magnetics* 49, no. 4 (2012): 1461–1469, https://doi.org/10.1109/tmag.2012.2227147.

10. S. Ishii, Y. Hasegawa, K. Nakamura, and O. Ichinokura, "Novel Flux Barrier Type Outer Rotor IPM Motor With Rare-Earth and Ferrite Magnets," *Journal of the Magnetics Society of Japan* 37, no. 3–2 (2013): 259–263, https://doi.org/10.3379/msjmag.1305r004.

11. I. Afinowi, Z. Q. Zhu, Y. Guan, J. C. Mipo, and P. Farah, "Performance Analysis of a Switched-Flux Permanent Magnet Machine With Hybrid NdFeB and Ferrite Magnet," in *The 17th Int. Conf. on Electrical Machines and Systems, ICEMS2014, Hangzhou, China* (October 2014), 3110–3116.

12. Y. Chen, T. Cai, X. Zhu, and Y. Ding, "Optimization of a New Asymmetric-Hybrid-PM Machine With High Torque Density and Low Torque Ripple Considering the Difference of Magnetic Materials," *IEEE Transactions on Magnetics* 58, no. 2 (2021): 1–5.

13. S. Kazemisangdehi, Z. Q. Zhu, and Y. J. Zhou, "Split Spoke Series Hybrid PM Delta-Shape IPMSM With Improved Performance," in *2023 26th Int. Conf. On Electrical Machines and Systems (ICEMS)* (IEEE, 2023), 678–683.

14. A. Al-Qarni and A. El-Refaie, "Magnetic Gears and Magnetically Geared Machines With Reduced Rare-Earth Elements for Vehicle Applications," *World Electric Vehicle Journal* 12, no. 2 (2021): 52, https://doi.org/10.3390/wevj12020052.

15. Y. Chen, X. Zhou, Z. Li, and X. Zhu, "Torque Performance Enhancement for Hybrid PM Motor Considering Magnet Characteristic Difference and Variation," *IEEE Transactions on Magnetics* 59, no. 11 (2023): 1–5, https://doi.org/10.1109/tmag.2023.3278306.

16. S. Zheng, X. Zhu, L. Xu, Z. Xiang, L. Quan, and B. Yu, "Multi-Objective Optimization Design of a Multi-Permanent-Magnet Motor Considering Magnet Characteristic Variation Effects," *IEEE Transactions on Industrial Electronics* 69, no. 4 (2021): 3428–3438, https://doi.org/10.1109/tie.2021.3073311.

17. Z. S. Du and T. A. Lipo, "Cost-Effective High Torque Density Bi-Magnet Machines Utilizing Rare Earth and Ferrite Permanent Magnets," *IEEE Transactions on Energy Conversion* 35, no. 3 (2020): 1577–1584, https://doi.org/10.1109/tec.2020.2978256.

18. Q. Ma, A. El-Refaie, and B. Lequesne, "Low-Cost Interior Permanent Magnet Machine With Multiple Magnet Types," *IEEE Transactions on Industry Applications* 56, no. 2 (2020): 1452–1463, https://doi.org/10.1109/tia.2020.2966458.

19. S. Kazemisangdehi, Z. Q. Zhu, Y. Zhou, H. Liu, L. Chen, and L. Yang, "Novel Parallel Hybrid Rare-Earth and Ferrite Magnets in V-Spoke Interior PM Synchronous Machine," *IEEE Transactions on Industry Applications* 61, no. 2 (2025): 2972–2982, https://doi.org/10.1109/tia.2024.3524978.

20. X. Zeng, L. Quan, X. Zhu, L. Xu, and F. Liu, "Investigation of an Asymmetrical Rotor Hybrid Permanent Magnet Motor for Approaching

Maximum Output Torque," *IEEE Transactions on Applied Superconductivity* 29, no. 2 (2019): 1–4, https://doi.org/10.1109/tasc.2019.2893708.

21. X. Zhu, S. Li, S. Zheng, et al., "Torque Component Redistribution and Enhancement for Hybrid Permanent Magnet Motor With Permanent Magnet Offset Placement," *IEEE Transactions on Transportation Electrification* 9, no. 1 (2022): 631–641, https://doi.org/10.1109/tte.2022.3177745.

22. Z. Qiao, L. Shi, F. Li, H. Xu, T. Zhou, and W. Wang, "Characteristics Analysis of Magnetic-Pole-Shift in an Asymmetric Hybrid Pole-Permanent Magnet Assisted Synchronous Reluctance Motor," *IEEE Journal of Emerging and Selected Topics in Power Electronics* 13, no. 2 (2024): 1394–1405.

23. G. Xu, G. Liu, X. Du, and F. Bian, "A Novel PM Motor With Hybrid PM Excitation and Asymmetric Rotor Structure for High Torque Performance," *AIP Advances* 7, no. 5 (2017): 056671, https://doi.org/10.1063/1.4978400.

24. Y. Ji, Y. Li, and Q. Lu, "Investigation of a Novel Hybrid Less-Rare-Earth Consequent-Pole Interior Permanent Magnet Machine With Asymmetric Rotor," in *2023 26th Int. Conf. On Electrical Machines and Systems (ICEMS)* (IEEE, 2023), 5354–5359.

25. L. Liu, Y. Ma, K. Shuai, et al., "A Comparative Study of V-Shaped IPMSMs With Asymmetric and Symmetric Rotors," in *2024 the 9th International Conference on Power and Renewable Energy (ICPRE)* (IEEE, 2024), 108–113.

26. K. Liu, L. Shi, Z. Liu, W. Wang, and H. Ding, "Analysis and Optimization of Asymmetric Hybrid Permanent Magnet Motor for Electric Vehicle," *Journal of Electrical Engineering and Technology* 18, no. 5 (2023): 3555–3567, https://doi.org/10.1007/s42835-023-01418-x.

27. W. Chu and Z. Q. Zhu, "Average Torque Separation in Permanent Magnet Synchronous Machines Using Frozen Permeability," *IEEE Transactions on Magnetics* 49, no. 3 (2012): 1202–1210, https://doi.org/10.1109/tmag.2012.2225068.

28. T. Burress, "Benchmarking State-of-the-Art Technologies," in *Oak Ridge National Laboratory (ORNL), 2013 US DOE Hydrogen and Fuel Cells Program and Vehicle Technologies Program Annual Merit Review and Peer Evaluation Meeting* (2013).

29. T. A. Huynh and M.-F. Hsieh, "Comparative Study of PM-Assisted SynRM and IPMSM on Constant Power Speed Range for EV Applications," *IEEE Transactions on Magnetics* 53, no. 11 (2017): 1–6, https://doi.org/10.1109/intmag.2017.8008078.

30. X. Zhu, X. Wang, C. Zhang, L. Wang, and W. Wu, "Design and Analysis of a Spoke-Type Hybrid Permanent Magnet Motor for Electric Vehicles," *IEEE Transactions on Magnetics* 53, no. 11 (2017): 1–4, https://doi.org/10.1109/tmag.2017.2701146.

31. R. Yang, "Electrified Vehicle Traction Machine Design With Manufacturing Considerations," (PhD dissertation, College of Mechanical Engineering, McMaster University, 2016), [Online], accessed July 28, 2021, https://macsphere.mcmaster.ca/bitstream/11375/20895/2/Yang_Rong_2016December_Ph.D..pdf.

32. J. Hemsen, N. Nowak, and L. Eckstein, "Production Cost Modeling for Permanent Magnet Synchronous Machines for Electric Vehicles," *Automotive and Engine Technology* 8, no. 2 (2023): 109–126, https://doi.org/10.1007/s41104-023-00128-w.

33. Z. Q. Zhu, "A Simple Method for Measuring Cogging Torque in Permanent Magnet Machines," in *2009 IEEE Power & Energy Society General Meeting* (IEEE, 2009), 1–4.